



Relationship between capillary pressure, saturation, and interfacial area from a model of mixed-wet triangular tubes

J. O. Helland¹ and S. M. Skjæveland²

Received 1 November 2006; revised 27 June 2007; accepted 10 July 2007; published 30 November 2007.

[1] A simple bundle of triangular tubes model is employed to calculate specific interfacial area for primary drainage, imbibition, and secondary drainage for mixed-wet conditions. In this model, only the interfaces between bulk and corner fluid are contributory to the interfacial area. Accurate expressions for the capillary entry pressures are employed, which account for the possibility of hinging interfaces in the corners due to contact angle hysteresis. The results show that very different trends in the specific interfacial area versus saturation curves can occur during imbibition, depending on the advancing contact angle and the reversal point after primary drainage. For water-wet conditions, interfacial area scanning curves coincide with the bounding imbibition curve, while for oil-wet conditions, the scanning curves may cross each other because of the impact that hinging interfaces in the pore corners have on the invasion order of the pore sizes. Analytical expressions for specific interfacial area as a function of saturation and capillary pressure are derived for primary drainage of triangular tubes. Approximate correlations for interfacial area as a function of saturation are suggested for the subsequent imbibition and drainage processes. The correlations are fitted to the simulated data, and good agreement is obtained. We also demonstrate that hysteresis remains present in the relationship between interfacial area, capillary pressure, and saturation when contact angle hysteresis is assumed. Hysteresis may be significant for both water-wet and mixed-wet conditions. A more sophisticated model is required to examine if this is also the case when hysteresis is caused by phase entrapment.

Citation: Helland, J. O., and S. M. Skjæveland (2007), Relationship between capillary pressure, saturation, and interfacial area from a model of mixed-wet triangular tubes, *Water Resour. Res.*, 43, W12S10, doi:10.1029/2006WR005698.

1. Introduction

[2] Fluid-fluid interfacial area is recognized in the literature as an important parameter in understanding various multiphase flow processes in porous media. Mass transfer processes such as dissolution, adsorption and volatilization occur across interfaces and are strongly related to interfacial area. In particular, the coefficient for interfacial mass transfer rate is assumed to be proportional to the interfacial area [e.g., Kennedy and Lennox, 1997]. It has also been observed experimentally that surfactants and bacteria may preferentially accumulate at the fluid-fluid interfaces and affect the subsequent fluid transport [e.g., Schäfer et al., 1998]. Thus the magnitude of the interfacial area is needed to quantify the efficiency and consequences of these processes.

[3] Specific interfacial area between phase i and j is defined as

$$a_{ij} = \frac{1}{\mathcal{V}} \int_{\mathcal{S}_{ij}} d\mathcal{S}, \quad (1)$$

where \mathcal{V} is a representative volume including both phases and \mathcal{S}_{ij} is the total area of the interfaces in \mathcal{V} .

[4] Despite the difficulties involved in direct measurements of the parameter a_{ij} as a function of saturation in porous media, progress has been made the last 10 a to develop more reliable experimental methods. Saripalli et al. [1998]; Schaefer et al. [2000a] and Faisal Anwar et al. [2000] employed interfacial tracer techniques to determine the two-phase interfacial area using water-soluble surfactants. The mass of surfactant adsorbed at the interfaces was determined, and the Gibbs adsorption equation was employed together with measurements of interfacial tensions to calculate the interfacial area. Schaefer et al. [2000b] used the same approach to determine three-phase interfacial area.

[5] Pore-scale modeling represents an appealing approach to estimate the interfacial area explicitly and to study its functional dependencies. This is mainly due to the possibility of calculating several key parameters for multiphase flow simultaneously, which may be difficult or even impossible to obtain from experimental measurements. Reeves and Celia [1996] calculated the specific interfacial area between bulk fluids in a network constructed by conical pore throats of circular cross sections. More recently, networks of angular pore shapes have been used to include the

¹International Research Institute of Stavanger, Stavanger, Norway.

²Department of Petroleum Engineering, University of Stavanger, Stavanger, Norway.

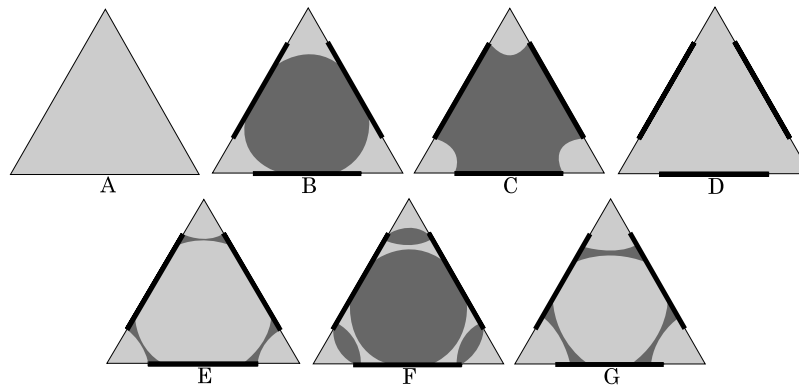


Figure 1. Fluid configurations for primary drainage, imbibition, secondary drainage, and secondary imbibition, with water in light gray and oil in dark gray. The bold lines along the sides represent lengths of the pore walls where the wettability may have changed.

contribution of interfacial area from fluid-fluid interfaces in the corners of the pore space [Dillard *et al.*, 2001; Dalla *et al.*, 2002]. Or and Tuller [1999] and Gladkikh and Bryant [2003] have in addition included the area of thin films coating the pore walls in the calculations.

[6] Other methods to calculate the interfacial area focus on the relationship between capillary pressure and saturation ($P_c - S$). On the basis of thermodynamics, Bradford and Leij [1997] estimated two- and three-phase interfacial area from measured $P_c - S$ data. Ostrom *et al.* [2001] derived analytical expressions for free and entrapped interfacial area as functions of water saturation by assuming the Brooks-Corey [Brooks and Corey, 1964] and the van Genuchten [van Genuchten, 1980] correlations for the $P_c - S$ relationship. The estimated expressions were in good agreement with experimental measurements.

[7] Hassanizadeh and Gray [1993] argued that there exists a formal constitutive relationship between capillary pressure, saturation and specific interfacial area. They hypothesized that hysteresis in the $P_c - S$ relationship is an artifact of projecting the $a_{ij} - P_c - S$ surface onto the $P_c - S$ plane. New macroscopic theories for multiphase flow have subsequently been developed that require the $a_{ij} - P_c - S$ relationship [e.g., Gray, 1999]. Reeves and Celia [1996] investigated the conjecture of Hassanizadeh and Gray [1993] with their network model. The a_{ij} surfaces plotted as a function of P_c and S displayed a characteristic convex shape which indicated that the functional relationship is nonunique, e.g., for any value of capillary pressure there corresponds at least two points on the surface with different saturations and the same specific interfacial area. Held and Celia [2001] calculated the a_{ij} surfaces with another network model, and the same convex shape was observed. They simulated imbibition and drainage scanning curves to cover the entire area within the bounding hysteretic $P_c - S$ loop and found a small separation between the imbibition and drainage a_{ij} surfaces. Thus they concluded that hysteresis was essentially eliminated in their numerical experiments. However, they only calculated interfacial area between the bulk fluids for water-wet conditions and hence neglected the impact of mixed wettability and corner fluid occupancy.

[8] In this paper we use a physically based capillary bundle model of triangular tubes to calculate two-phase oil-water specific interfacial area for mixed-wet conditions. Although such a representation is simplistic as it does not account for the interconnectivity of real porous media, the model has been shown to reproduce main features of two-phase capillary pressure curves for mixed-wet rock, scanning loops included [Helland and Skjæveland, 2006]. On the basis of the triangular pore geometry, we derive analytical expressions for the specific interfacial area as a function of saturation and capillary pressure for primary drainage and propose approximate correlations for the specific interfacial area for subsequent imbibition and drainage processes. The correlations are compared with simulated data. Finally, we challenge the conjecture of Hassanizadeh and Gray [1993] and explore if hysteresis can be eliminated for mixed-wet drainage and imbibition $P_c - S$ curves when specific interfacial area is incorporated in the relationship.

2. Model Description

[9] We employ a pore-scale model with a bundle of tubes representation of the pore network, the tubes having equilateral, triangular cross sections. This pore geometry is readily described by the half angle of the corner, $\alpha = \pi/6$, and the inscribed radius R . The angular pore shape allows for representation of physical processes such as the establishment of mixed wettability within a single pore and drainage through fluid layers in the corners of the pore space [e.g., Kovscek *et al.*, 1993; Hui and Blunt, 2000]. In this section we review the aspects of the model which is relevant for the calculation of the specific interfacial area. The model is described in detail elsewhere [Helland and Skjæveland, 2006].

[10] The cross-sectional fluid configurations that may occur in a tube for the sequence of processes primary drainage, imbibition, secondary drainage and secondary imbibition are shown in Figure 1. The curvatures of the interfaces in the corners are allowed to be positive or negative depending on the contact angles and the capillary pressure. Configuration A shows a tube that always has been water filled, while configuration B–G represent tubes that at some point have been invaded by oil. The bold lines

indicate the lengths of the pore walls that have been contacted by oil and hence may have altered wettability after primary drainage. The distance b_{pd} from the apex of the corner to the position of the contact line at the end of primary drainage remains water-wet:

$$b_{pd} = \frac{\sigma_{ow} \cos(\theta_{pd} + \alpha)}{P_c^{\max} \sin \alpha}, \quad (2)$$

where θ_{pd} is the contact angle, and P_c^{\max} is the capillary pressure at the end of primary drainage.

[11] Configuration B and C may occur for the first time during water flooding when the water content in the corners has started to increase after primary drainage. Water invasion into configuration B is always a displacement to configuration D, while water invasion into configuration C is a displacement to configuration D or E. Configuration F may occur during secondary drainage when oil invades configuration E. Configuration G may occur for the first time during secondary imbibition when configuration B is invaded by water. Additionally, the layer displacements E to D and G to D may occur during imbibition, whereas the layer displacements F to C and D to E may occur during drainage [van Dijke and Sorbie, 2006; Helland and Skjæveland, 2006]. To restrict the number of possible configurations, we do not allow formation of additional interfaces in configuration F and G during subsequent saturation reversals. In theory, although not very likely, the number of interfaces in a cross section could increase as saturation reversals proceed, provided that contact angle hysteresis is large.

[12] It is well known that contact angle hysteresis can occur because of roughness of the pore walls and microscopic wetting heterogeneity [e.g., Morrow, 1975; Paterson *et al.*, 1998]. Instead of modeling these details explicitly, we assume that any effects can be accounted for by using contact angles that depend on the direction of the process. To account for contact angle hysteresis and wettability alteration we use a small receding contact angle θ_{pd} in primary drainage, an advancing contact angle θ_a in imbibition, and a receding contact angle θ_r in secondary drainage, which satisfy $\theta_{pd} \leq \theta_r \leq \theta_a$. Throughout this work, the contact angles are always measured through the denser phase (water).

[13] In processes after primary drainage, new interfaces form at positions $b > b_{pd}$ in the corners only for limited values of the contact angle θ of the interface that separates the bulk fluids. When bulk oil displaces water in an oil flood, interfaces between bulk oil and water in layers can form only if

$$\theta < \frac{\pi}{2} - \alpha, \quad (3)$$

where θ is equal to the receding contact angle θ_r . However, if equation (3) is not satisfied for θ_r , the interfaces still form with a hinging contact angle $\theta_h > \theta_r$ at position $b = b_{pd}$. Similarly, when bulk water displaces oil in a water flood, new interfaces between bulk water and oil in layers can form only if

$$\theta > \frac{\pi}{2} + \alpha, \quad (4)$$

where θ is equal to θ_a . Additionally, the layer displacement from configuration D to E during secondary drainage is only possible if θ_r satisfies equation (4).

[14] The capillary pressure across an interface in a corner is given by

$$P_c \equiv P_o - P_w = \frac{\sigma_{ow}}{r}, \quad (5)$$

where r is the radius of curvature measured through the oil phase such that $r > 0$ when $P_c > 0$.

[15] To efficiently handle configurations with more than one interface present in the corner, we introduce some notation. Interfaces are numbered in order from the corner toward the center of the cross section. We apply the indicator notation

$$I^{(k)} = \begin{cases} 1 & \text{if interface } k \text{ separates} \\ & \text{bulk oil and corner water} \\ -1 & \text{if interface } k \text{ separates} \\ & \text{bulk water and corner oil.} \end{cases} \quad (6)$$

Furthermore, the total number of interfaces present in a corner before a piston-like displacement is denoted N^{init} , while the total number of interfaces after the displacement is denoted N^{fin} . The cross-sectional bulk area bounded by interface k is denoted $A_b^{(k)}$. The bounding solid-fluid and oil-water lengths are denoted $L_s^{(k)}$ and $L_f^{(k)}$, respectively. These parameters are defined as follows:

$$A_b^{(k)} = \begin{cases} 3R^2 \cot \alpha - 3rb^{(k)} \sin(\beta^{(k)} + \alpha) + 3r^2 \beta^{(k)} & \text{if } I^{(k)} = 1 \\ 3R^2 \cot \alpha - 3rb^{(k)} \sin(\beta^{(k)} - \alpha) - 3r^2 \beta^{(k)} & \text{if } I^{(k)} = -1 \end{cases} \quad (7)$$

$$L_f^{(k)} = 6r\beta^{(k)} \quad (8)$$

and

$$L_s^{(k)} = 6R \cot \alpha - 6b^{(k)}, \quad (9)$$

where

$$b^{(k)} \sin \alpha = r \sin \beta^{(k)} \quad (10)$$

and

$$\beta^{(k)}(\theta^{(k)}) = \begin{cases} \frac{\pi}{2} - \alpha - \theta^{(k)} & \text{if } I^{(k)} = 1 \\ \frac{\pi}{2} + \alpha - \theta^{(k)} & \text{if } I^{(k)} = -1. \end{cases} \quad (11)$$

Equations (7)–(11) are written with general contact angles $\theta^{(k)}$ that may be equal to $\theta_h^{(k)}$ if the interface is hinging, θ_r if the interface is receding, or θ_a if the interface is advancing. Notice also that $b^{(1)} = b_{pd}$ in configuration C, E and F.

[16] After a reversal of saturation change, the interfaces in the corners, if present, may be stuck at fixed positions while

the contact angle changes with capillary pressure. Using equations (5), (10) and (11), interface k hinges according to

$$\theta_h^{(k)} = \begin{cases} \arccos\left(\frac{P_c b^{(k)} \sin \alpha}{\sigma_{ow}}\right) - \alpha & \text{if } I^{(k)} = 1 \\ \arccos\left(\frac{P_c b^{(k)} \sin \alpha}{\sigma_{ow}}\right) + \alpha & \text{if } I^{(k)} = -1. \end{cases} \quad (12)$$

If the advancing or receding contact angle is reached prior to piston-like invasion, the interfaces in the corners begin to move at constant contact angles during a further change of capillary pressure. The position $b^{(k)}$ of interface k is then changing according to

$$b^{(k)} = \begin{cases} \frac{\sigma_{ow} \cos(\theta^{(k)} + \alpha)}{P_c \sin \alpha} & \text{if } I^{(k)} = 1 \\ \frac{\sigma_{ow} \cos(\theta^{(k)} - \alpha)}{P_c \sin \alpha} & \text{if } I^{(k)} = -1, \end{cases} \quad (13)$$

where $\theta^{(k)}$ is equal to θ_{pd} in primary drainage, θ_a in imbibition, and θ_r in secondary drainage.

2.1. Capillary Entry Pressures

[17] The capillary entry pressures for piston-like invasion are calculated from an energy balance equation which equates the virtual work with the associated change in surface free energy for a small displacement of the invading interface in the direction along the tube length. This energy balance arises from a minimization of the change in total Helmholtz free energy of the system (capillary tube) and the surroundings (oil and water reservoirs), i.e., $dF_H = 0$, which is the condition for thermodynamic equilibrium in isothermal systems of constant total volume. By further assuming incompressible fluids, reversible displacements and constant chemical potentials, the minimization of the change in Helmholtz free energy is given by [e.g., *Morrow, 1970; Bradford and Leij, 1997*]

$$dF_H = -W + dF = -\sum_{i=o,w} P_i dV_i + \sum_{ij=ow,os} \sigma_{ij} dA_{ij} = 0, \quad (14)$$

where W is the work done on the system, dF is the corresponding change in surface free energy of the system, dV_i is the change in fluid volumes, and dA_{ij} represent the changes in area of the oil-water and fluid-solid interfaces. Using Young's equation, $\sigma_{os} - \sigma_{ws} = \sigma_{ow} \cos \theta$, and the definition of capillary pressure, equation (14) can be written as

$$P_c dV_o = \sigma_{ow} (dA_{ow} + \cos \theta dA_{os}). \quad (15)$$

For a capillary tube, the energy balance equation (15) relates the effective entry radius of curvature, expressed by r , to the cross-sectional area exposed to change of fluid occupancy, the bounding cross-sectional fluid-solid and fluid-fluid lengths, and the contact angle θ of the interface that separates the two bulk fluids [e.g., *Ma et al., 1996; Øren et al., 1998*]. To account for all the allowed displacements between configurations A–G (both bulk and layer displacements), equation (15) may be formulated as follows using the notation from equations (5)–(11):

ments), equation (15) may be formulated as follows using the notation from equations (5)–(11):

$$\begin{aligned} & \frac{1}{r} \left(\sum_{k=1}^{N^{fin}} A_b^{(k)} I^{(k)} - \sum_{k=1}^{N^{init}} A_b^{(k)} I^{(k)} \right) \\ &= \cos \theta \left(\sum_{k=1}^{N^{fin}} L_s^{(k)} I^{(k)} - \sum_{k=1}^{N^{init}} L_s^{(k)} I^{(k)} \right) \\ &+ \left(\sum_{k=1}^{N^{fin}} L_f^{(k)} - \sum_{k=1}^{N^{init}} L_f^{(k)} \right). \end{aligned} \quad (16)$$

where θ is equal to θ_{pd} , θ_a and θ_r for primary drainage, imbibition and secondary drainage, respectively.

[18] If invasion occurs while the interfaces in the corners hinge at fixed positions $b^{(k)}$, then $\theta^{(k)} \neq \theta$, and equation (16) is solved iteratively together with equations (7)–(10) to obtain a converged value of r . When $\theta^{(k)} = \theta$, explicit expressions for r are derived by combining equations (7)–(11) and (16). This is always the case in primary drainage where $\theta^{(1)} = \theta_{pd}$. The capillary entry pressure is finally calculated from equation (5).

[19] Generally, piston-like invasion in a given pore can occur by different scenarios of configuration changes based on the values of the contact angles. To determine the correct displacement, the different scenarios and the associated entry pressures must be analyzed. The actual displacement occurring is the one with the most favorable entry pressure among the geometrically possible scenarios. The procedure which determines the actual displacements occurring in each case is presented in detail elsewhere [*Helland and Skjæveland, 2006*].

2.2. Consistency of the Entry Pressures

[20] All the configurations depicted in Figure 1 have previously been incorporated in pore-scale models [e.g., *Piri and Blunt, 2005; Helland and Skjæveland, 2006*]. However, only for configuration A–E has it been demonstrated that the entry pressures calculated from the energy balance equation (15) are consistent [*van Dijke and Sorbie, 2006*]. This implies that, for a given pore, there is a unique relation between capillary pressure and fluid configuration in the absence of hysteresis. By considering the water flood after primary drainage in a star-shaped pore, *van Dijke and Sorbie* [2006] demonstrated that the entry pressures for the configuration changes from C to E and E to D are consistent with the direct displacement from C to D on a plot of capillary pressure versus a chosen parameter, for example θ_a . This implies that the three entry pressures meet in a unique crossover and define three distinct (θ_a, P_c) regions which correspond uniquely to configuration C, D and E. Moreover, in the entire range of the chosen parameter θ_a , the different parts of the three entry pressure curves which are relevant and favorable, constitute continuous functions [*van Dijke and Sorbie, 2006*].

[21] In the following, we show that a similar consistency appears for configurations C, E and F during secondary drainage and that configuration F may form. We analyze a pore size $R = 100 \mu\text{m}$ with a displacement history composed of primary drainage followed by a water flood. The interfacial tension is set as $\sigma_{ow} = 0.020 \text{ N/m}$. Primary drainage is terminated at $P_c^{\text{max}} = 50 \text{ kPa}$, and the subsequent water flood is terminated at different capillary pressure values P_c^{min} from which the entry pressures for the secondary drainage pro-

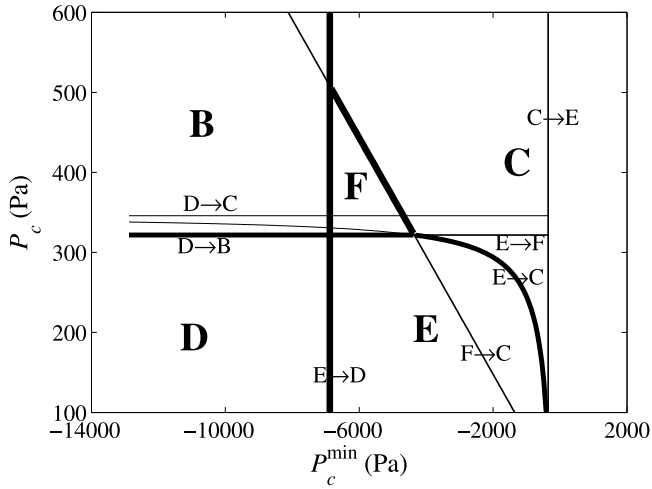


Figure 2. Capillary entry pressures for secondary drainage plotted as a function of capillary pressure at the end of the preceding water flood. The vertical lines represent the entry pressures during the water flood. The bold lines represent the relevant parts of the entry pressures which define the regions of configurations B–F.

cess are calculated. The contact angles used are $\theta_{pd} = 0^\circ$, $\theta_a = 180^\circ$ and $\theta_r = 30^\circ$. These values allow formation of configuration F in the secondary drainage process from a pure geometrical point of view. Thus we choose to study consistency in the (P_c^{\min}, P_c) plane with constant receding and advancing contact angles. The results are presented in Figure 2. The vertical lines represent the entry pressures during the water flood. The displacement C to E occurs first, followed by the displacement E to D at a smaller value of P_c^{\min} . In the range of P_c^{\min} where configuration E exists, oil invasion during secondary drainage occurs by a direct displacement to configuration C for large P_c^{\min} , while for smaller P_c^{\min} the displacement E to F occurs first followed by the displacement F to C. Notice that the entry pressures for these displacements are consistent; that is, they meet in a unique crossover and define three distinct regions of configuration C, E and F such that the relevant parts of the entry pressures constitute continuous functions in the range of P_c^{\min} where configuration E exists initially.

[22] The entry pressures for the displacements D to B, B to C and D to C in secondary drainage are also calculated consistently. The entry pressure for displacement B to C is very high and is therefore not included in the plot. These entry pressures appear as horizontal lines as they do not depend on P_c^{\min} . Thus, to demonstrate consistency in this case, it would be better to study the (P_c^{\max}, P_c) plane, as the displacements B to C and C to D both depend on P_c^{\max} .

[23] A large discontinuity of the oil flood entry pressures occurs at the value of P_c^{\min} which corresponds to the water flood entry pressure for the displacement from configuration E to D. A consequence of this behavior is that discontinuous steps can occur in the $P_c(S_w)$ curves calculated from the capillary bundle model. An oil flood initiated in the range of P_c^{\min} where configuration E exists will form configuration C at a much smaller capillary pressure than an oil flood initiated from the range where configuration D exists. In the latter case configuration B forms instead, and a large

pressure is required to form configuration C. This “inconsistency” is caused by the contact angle hysteresis. The water flood entry pressures are calculated with advancing contact angles, while the oil flood entry pressures are calculated with receding contact angles, which implies that the entry pressures for the different processes do not fit in with each other. We are uncertain as to whether this inconsistency represents a physical property of capillary systems with contact angle hysteresis or if it occurs because of an insufficient understanding of how contact angle hysteresis should be represented. However, the entry pressures for each process are calculated consistently “configuration by configuration”. In this example, all the relevant entry pressures for configuration E are consistent, and the same is true for the entry pressures calculated in the range where configuration D exists initially. The discontinuity appears when these two cases are put together as a whole.

[24] Similar calculations performed for configuration B during the secondary water flood show that the entry pressures for the displacements B to G, G to D and B to D are consistent, and that configuration G may form. This scenario is not analyzed here as it is very similar to what *van Dijke and Sorbie* [2006] presented for displacements C to E, E to D and C to D for the first water flood after primary drainage.

3. Calculation of Interfacial Area

[25] Since we assume a capillary bundle model of straight triangular tubes, it suffices to consider the cross sections when calculating saturation and specific interfacial area. The cross-sectional area A of a tube is related to the radius of the inscribed circle, R , by

$$A = 3R^2 \cot \alpha. \quad (17)$$

To calculate the area of oil and water occupied in corner regions and layers we use combinations of the following equation with appropriate arguments ψ :

$$A_c(\psi) = 3r^2 \left(\psi + \alpha - \frac{\pi}{2} + \cos \psi \left(\frac{\cos \psi}{\tan \alpha} - \sin \psi \right) \right). \quad (18)$$

As an example, the area of water in the corners of configuration C is given by $A_c(\theta_h^{(1)})$, whereas the area of oil in layers of configuration E is calculated from $A_c(\pi - \theta_a) - A_c(\theta_h^{(1)})$ when the interfaces bounding bulk water are advancing toward the corners. Thus equations (17) and (18) constitute the expressions required to calculate the saturation.

[26] Specific interfacial area is calculated from equation (1) by adding the lengths of all oil-water interfaces in the corners of the tubes and dividing by the total cross-sectional tube area in the bundle. The interfacial lengths are readily expressed in terms of equation (8) with the appropriate values for $\beta^{(k)}(\theta^{(k)})$:

$$L_f^{(k)} = 6r\beta^{(k)}(\theta^{(k)}). \quad (19)$$

As an example, the interfacial length in configuration C with hinging interfaces is $6r\beta^{(1)}(\theta_h^{(1)})$. The interfacial length in configuration E is given by $6r\beta^{(1)}(\theta_h^{(1)}) + 6r\beta^{(2)}(\theta_a)$ if the

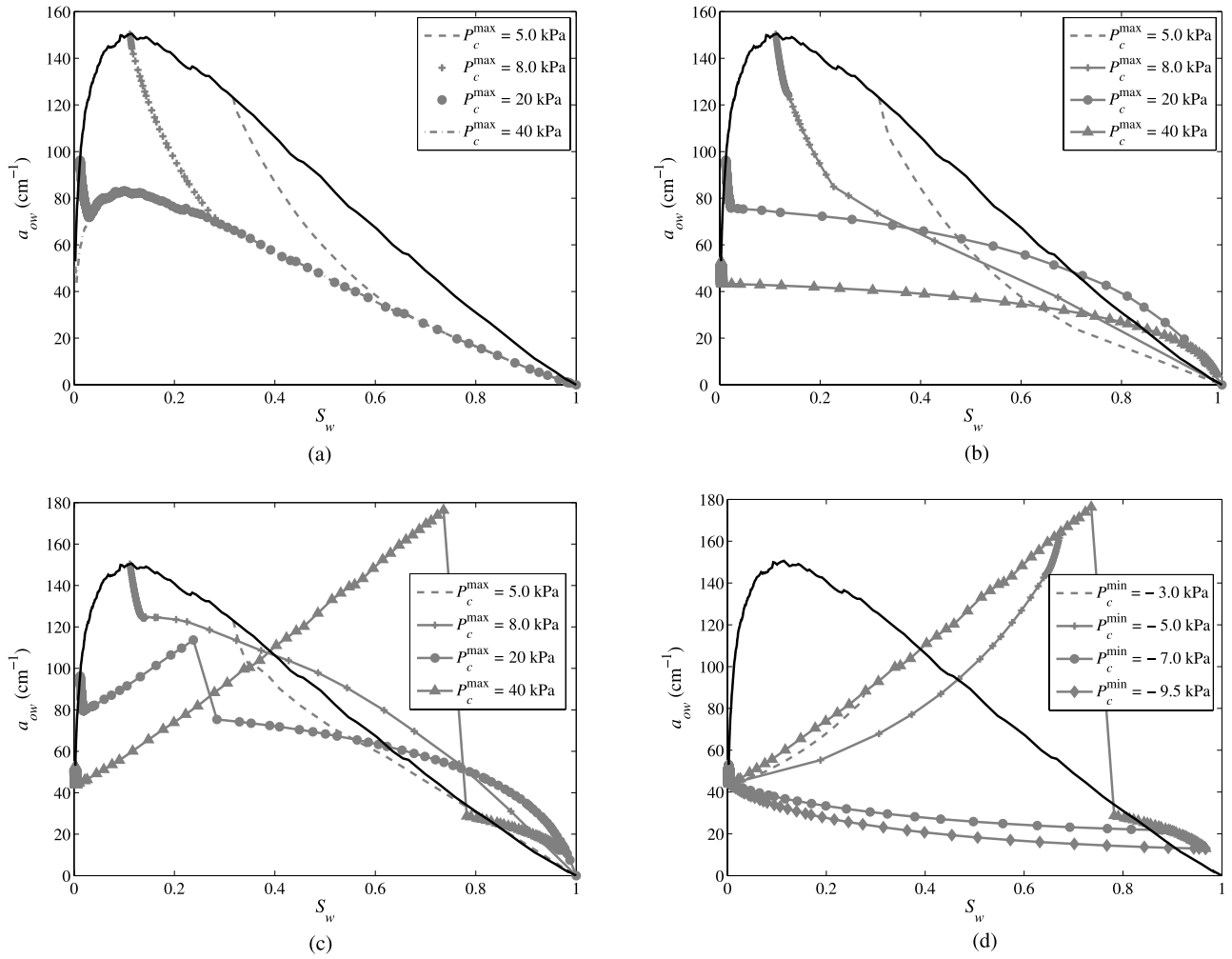


Figure 3. Specific interfacial area plotted versus saturation. Imbibition scanning curves from different reversal points after primary drainage with (a) $\theta_a = 30^\circ$, (b) $\theta_a = 120^\circ$, and (c) $\theta_a = 180^\circ$. (d) Effect of reversal point after imbibition on secondary drainage with $\theta_a = 180^\circ$, $\theta_r = 70^\circ$.

interfaces surrounding bulk water advance toward the corners. Since the model only accounts for cross-sectional configurations, it is not possible to calculate interfacial area between bulk phases. Moreover, we neglect the contribution to interfacial area from possible thin films along the sides of the tubes.

3.1. Numerical Examples

[27] We have performed simulations of the specific interfacial area versus saturation relationship for primary drainage, imbibition and secondary drainage. For this purpose we assume that the pore size density is described by a truncated Weibull distribution [Dong *et al.*, 1995; Hui and Blunt, 2000]. The pore sizes R are generated in the following manner: Pick random numbers $x \in [0, 1]$ and calculate inscribed radii from

$$R = R_{ch} \left(-\ln \left[(1-x) \exp \left(-\left[\frac{R_{max} - R_{min}}{R_{ch}} \right]^\eta \right) + x \right] \right)^{\frac{1}{\eta}} + R_{min}, \quad (20)$$

where R_{max} , R_{min} and R_{ch} are the inscribed radii of the largest, smallest and characteristic pore sizes, respectively,

and η is a dimensionless parameter. In the simulations we set $R_{min} = 0 \mu\text{m}$, $R_{max} = 100 \mu\text{m}$, $R_{ch} = 15 \mu\text{m}$ and $\eta = 1.5$. Furthermore, $\sigma_{ow} = 0.050 \text{ N/m}$ and $\theta_{pd} = 0^\circ$.

[28] Figures 3a–3c show imbibition specific interfacial area curves initiated from different saturation reversal points after primary drainage for three different advancing contact angles. The $a_{ow}(S_w)$ curve for primary drainage exhibits the same general trends as measured data [Faisal Anwar *et al.*, 2000; Schaefer *et al.*, 2000b; Oostrom *et al.*, 2001]. However, the shapes of the imbibition curves are very sensitive to the reversal point.

[29] Figure 3a shows results for water-wet conditions with $\theta_a = 30^\circ$. In this case, piston-like water invasion may occur by displacements from configuration C to D or from B to D. The displacement from C to D occurs while the interfaces in the corners hinge with a contact angle $\theta_h^{(1)} < \theta_a$ at position b_{pd} , and therefore the entry pressure depends on the P_c^{\max} value. This is different from the entry pressure for displacement B to D which does not depend on P_c^{\max} as the interfaces in the corners obtained the constant contact angle θ_a in the displacement from C to B prior to the piston-like invasion. The critical capillary pressure for displacement C to B, which represents the transition between the two

regimes of different displacements during the water flood, can easily be derived by comparing equation (2) and equation (13) with $b^{(1)} = b_{pd}$ and $\theta^{(1)} = \theta_a$. This results in the relation

$$P_c^{C \rightarrow B} = \frac{\cos(\theta_a + \alpha)}{\cos(\theta_{pd} + \alpha)} P_c^{\max}, \quad (21)$$

where θ_a satisfies equation (3) and $\theta_{pd} \leq \theta_a$. Equation (21) shows that $P_c^{C \rightarrow B}$ increases linearly with P_c^{\max} and that the displacement does not depend on pore size. If $P_c > P_c^{C \rightarrow B}$, displacements occur directly from configuration C to D. This behavior may dominate for small P_c^{\max} which corresponds to a large amount of water in the corners and a small $P_c^{C \rightarrow B}$. If $P_c < P_c^{C \rightarrow B}$, configuration B has formed, and piston-like invasion occurs by the displacement B to D. This behavior dominates for large P_c^{\max} which corresponds to large $P_c^{C \rightarrow B}$ values. Since water invades the pores in the order of increasing size during the imbibition process, the displacement from C to D occurs in the small pores, and when $P_c^{C \rightarrow B}$ is reached, the process proceeds in the larger pores by displacements from B to D. The differences in these trends are visible in the interfacial area curves starting at $P_c^{\max} = 5.0$ kPa and $P_c^{\max} = 8.0$ kPa where the displacement C to D occurs first. Subsequently, the displacement B to D occurs along the segments of the curves that coincide for the different P_c^{\max} values. This coincidence occurs because the corresponding entry pressures do not depend on P_c^{\max} . The imbibition curves originating from larger P_c^{\max} exhibit a steep decrease of interfacial area until a local minimum is reached. This decrease of a_{ow} is caused by the displacement from configuration C to D, which still occurs in a few of the smaller pores initially, and by the hinging of the interfaces in the corners of configuration C as P_c decreases. When $\theta_h^{(1)} = \theta_a$, configuration B forms, and the interfaces start to move toward the center of the pores with a constant contact angle θ_a . This results in a local increase of a_{ow} .

[30] Figure 3b demonstrates the effect of reversal point on imbibition interfacial area when $\theta_a = 120^\circ$. In this case, piston-like invasion always occurs by displacements from configuration C to D. In the initial stage, a_{ow} decreases steeply because of the hinging interfaces in configuration C. The displacement to configuration D is very sensitive to P_c^{\max} when $\theta_a > 90^\circ$, and invasion of the pore sizes may not necessarily occur in monotonically decreasing order, as demonstrated by *Helland and Skjæveland* [2006]. The fraction of water-wet pore-wall surface is larger in the smaller pores than in the larger ones since the distance b_{pd} does not depend on pore size. Thus the water in the corners, which is separated by hinging interfaces, affects the entry pressures increasingly as pore size decreases. For small P_c^{\max} , water preferentially invades the smaller pores first, which results in a pronounced decrease of interfacial area as water saturation increases. For larger P_c^{\max} , water preferentially invades the larger pore sizes first. As shown in Figure 3b, this results in a less pronounced decrease of interfacial area as a function of saturation. For intermediate values of P_c^{\max} , water may start to invade the larger and smaller pore sizes simultaneously [*Helland and Skjæveland*, 2006]. A consequence of the different invasion orders of the pore sizes for each imbibition process, which is caused by

the P_c^{\max} dependency on the entry pressures, is that the corresponding interfacial area scanning curves may cross each other, as shown in Figure 3b.

[31] Figure 3c shows the results for $\theta_a = 180^\circ$. The imbibition processes starting from $P_c^{\max} = 5.0$ kPa and $P_c^{\max} = 8.0$ kPa occur by displacements from configuration C to D. Thus the interfacial area curves display similar trends as observed in Figure 3b. However, for $P_c^{\max} = 20$ kPa and $P_c^{\max} = 40$ kPa, the displacement from configuration C to E occurs in the larger pores, which leads to a significant increase of a_{ow} . The interfacial area decreases abruptly when the layer displacement from configuration E to D occurs. Subsequently, the imbibition proceeds with displacements from configuration C to D, which results in a less pronounced decrease of a_{ow} .

[32] Figure 3d shows secondary drainage curves initiated from different reversal points along the imbibition curve with $P_c^{\max} = 40$ kPa in Figure 3c. The capillary pressures at the reversal points are denoted P_c^{\min} . In this example, the displacement from configuration E to C occurs for large values of P_c^{\min} . Because of the large contact angle hysteresis assumed ($\theta_a = 180^\circ$ and $\theta_r = 70^\circ$), this displacement occurs while the interfaces separating bulk water from oil in layers hinge. *Helland and Skjæveland* [2006] demonstrated that the invasion order of the pore sizes for this displacement is sensitive to P_c^{\min} when $\theta_r < 90^\circ$, and that the presence of oil layers tends to decrease the entry pressure. This trend is opposite to that observed for displacements between configuration D and C, where the presence of water in the corners tends to increase the entry pressure. In Figure 3d, the displacement E to C occurs preferentially in the order of increasing pore size, and hence the decrease of a_{ow} is most conspicuous at the initial stages of the drainage curves. For the small P_c^{\min} values, where configuration E has ceased to exist, invasion occur in the order of decreasing pore size, and the increase of interfacial area is most pronounced at the final stages of the drainage curves. Obviously, if a sufficiently small receding contact angle is considered, the displacement D to B will occur instead, implying that these drainage curves will resemble the general trends of the primary drainage curve. On the other hand, if θ_r is close to θ_a , the layer displacement D to E may occur instead, implying that the drainage curves will reproduce the complex shape of the imbibition curve.

3.2. Analytical Correlations for Primary Drainage

[33] To develop analytical expressions for specific interfacial area in primary drainage, we assume the simple pore size density

$$f(R) = \nu R_{\max}^{-\nu} R^{\nu-1}, \quad (22)$$

which includes the adjustable parameter $\nu > 0$. The uniform case corresponds to $\nu = 1$. *Helland and Skjæveland* [2006] have shown that this pore size density is compatible with the Brooks-Corey correlation if no water is residing in the corners after oil invasion, or if a bundle of cylindrical tubes model is assumed. The water saturation was expressed as a sum of two terms,

$$S_w = S_{wb} + S_{wc}, \quad (23)$$

where S_{wb} is the contribution from the tubes completely filled with water, and S_{wc} is the contribution from the tubes with water residing in the corners after invasion. It was found that

$$S_{wb} = \left(\frac{c}{P_c}\right)^{\nu+2}, \quad (24)$$

and

$$S_{wc} = \epsilon \frac{\nu+2}{\nu} \left(\frac{c}{P_c}\right)^2 \left[1 - \left(\frac{c}{P_c}\right)^\nu\right], \quad (25)$$

where ϵ is a geometry factor given by

$$\epsilon = \frac{g_1}{g_2}, \quad (26)$$

with

$$g_1(\theta_{pd}) = \cos \theta_{pd} - \sqrt{\frac{\tan \alpha}{2} (\sin 2\theta_{pd} - 2\theta_{pd} - 2\alpha + \pi)}, \quad (27)$$

and

$$g_2(\theta_{pd}) = \cos \theta_{pd} + \sqrt{\frac{\tan \alpha}{2} (\sin 2\theta_{pd} - 2\theta_{pd} - 2\alpha + \pi)}. \quad (28)$$

The capillary entry pressure c for the largest pore size R_{\max} is found by combining equations (7)–(11) with $\theta^{(1)} = \theta_{pd}$. This results in the relation

$$c = \frac{\sigma_{ow}}{R_{\max}} g_2. \quad (29)$$

By equation (24), capillary pressure may be expressed in terms of the bulk saturation as

$$P_c = c S_{wb}^{-a}, \quad (30)$$

where the pore size distribution index a is related to ν by

$$a = \frac{1}{\nu+2}. \quad (31)$$

If $S_{wc} = 0$, which corresponds to the case when no water is residing in the corners after oil invasion, the Brooks-Corey correlation [Brooks and Corey, 1964],

$$P_c = c S_w^{-a}, \quad (32)$$

is valid.

[34] To derive analytical expressions for the specific interfacial area, we employ the definition given by equation (1) as a starting point. For the bundle of triangular tubes, equation (1) yields

$$a_{ow} = \frac{L_f^{(1)} \int_{R_o}^{R_{\max}} f dR}{\int_0^{R_{\max}} f A dR}, \quad (33)$$

since the length $L_f^{(1)}$ is independent of pore size. The pore size invaded by oil at capillary pressure P_c is denoted R_o . By combining equations (7)–(11), we find that P_c is related to R_o by

$$R_o = \frac{\sigma_{ow}}{P_c} g_2. \quad (34)$$

Furthermore, with $L_f^{(1)} = 6r\beta^{(1)}(\theta_{pd})$ and $r = \sigma_{ow}/P_c$, equation (33) may be written as

$$a_{ow} = \frac{2c\beta^{(1)} \tan \alpha}{\sigma_{ow} g_2^2} \frac{\nu+2}{\nu} \frac{c}{P_c} \left[1 - \left(\frac{c}{P_c}\right)^\nu\right]. \quad (35)$$

Equation (35) relates specific interfacial area to capillary pressure. Equation (30) may be inserted into equation (35) to provide an equation which relates specific interfacial area to bulk water saturation:

$$a_{ow} = \frac{2c\beta^{(1)} \tan \alpha}{\sigma_{ow} g_2^2} \frac{\nu+2}{\nu} S_{wb}^{\frac{1}{\nu+2}} \left[1 - S_{wb}^{\frac{\nu}{\nu+2}}\right]. \quad (36)$$

Moreover, a comparison between equations (25), (35) shows that corner water saturation is related to specific interfacial area by

$$a_{ow} = \frac{2P_c\beta^{(1)} \tan \alpha}{g_1 g_2 \sigma_{ow}} S_{wc}. \quad (37)$$

[35] The analytically derived expressions imply that the $P_c - S_w$ and the $a_{ow} - S_w$ relationships are equivalent for primary drainage of triangular tubes. Equation (35) represents specific interfacial area as a function of only capillary pressure, i.e., $a_{ow} = F(P_c)$. Furthermore, equations (23)–(25) represents P_c as a function of S_w . Thus capillary pressure can be eliminated from these equations by means of the relationship $a_{ow} = F(P_c)$, which implies that equations (23)–(25) become a functional relationship between specific interfacial area and saturation instead.

[36] We have solved equations (23)–(25) and calculated specific interfacial area from equation (35) for different combinations of R_{\max} and ν . The results are presented in Figure 4. The level of specific interfacial area and capillary pressure is more sensitive to variations of R_{\max} than to variations of ν . The level of interfacial area is increased if the range of pore sizes is reduced. The $a_{ow}(S_w)$ curves exhibit the same general trends as measured primary drainage data [Faisal Anwar et al., 2000; Schaefer et al., 2000b; Oostrom et al., 2001].

3.3. Approximate Correlations for the Bounding Hysteresis Loop

[37] Since the bulk water saturation is much larger than the corner water saturation in most of the saturation range, we propose to formulate specific interfacial area as a function of total water saturation by employing the same functional form as given by equation (36). Different rock and fluid properties are accounted for by including adjust-

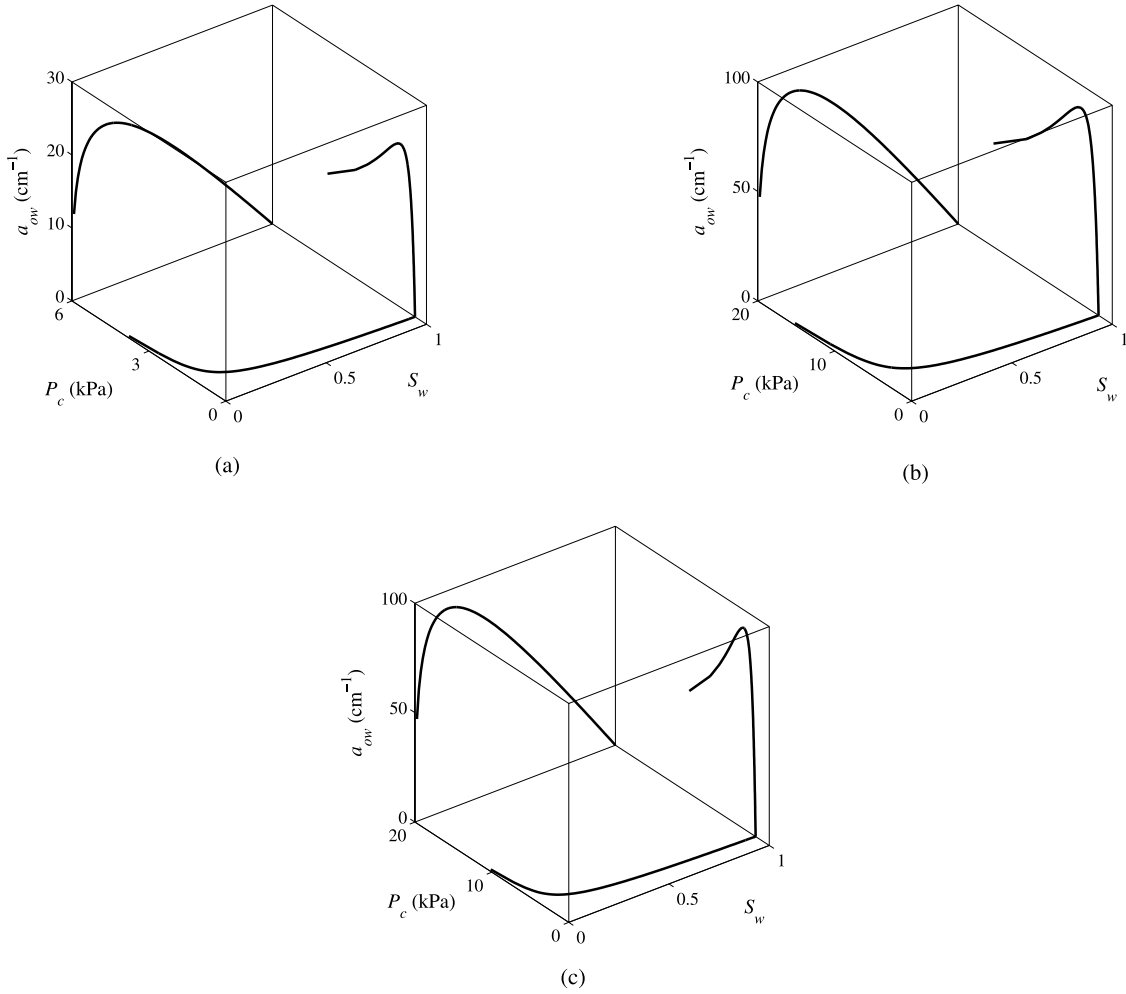


Figure 4. Primary drainage $a_{ow}(S_w)$, $a_{ow}(P_c)$ and $P_c(S_w)$ curves calculated from equations (23)–(25) and (35) using three different combinations of ν and R_{\max} : (a) $\nu = 0.5$, $R_{\max} = 200 \mu\text{m}$, (b) $\nu = 0.5$, $R_{\max} = 50 \mu\text{m}$ and (c) $\nu = 1.5$, $R_{\max} = 50 \mu\text{m}$.

able parameters. Thus, for water-wet media, we propose the correlation

$$a_{ow} = u_w S_w^{v_w} (1 - S_w^{q_w}), \quad (38)$$

where the three parameters u_w , v_w and q_w have to be determined. Obviously, u_w has the same dimension as specific interfacial area, whereas v_w and q_w are dimensionless.

[38] For water invasion into a complete oil-filled and oil-wet bundle of triangular tubes with equation (4) satisfied for θ_a , an expression similar to equation (36) can be derived where the bulk water saturation is replaced by the bulk oil saturation. For mixed-wet conditions we propose to formulate the interfacial area as a sum of two terms where one term is expressed by the water saturation, as in equation (38), while the other term is expressed by the oil saturation. This results in the correlation

$$a_{ow} = u_w S_w^{v_w} (1 - S_w^{q_w}) + u_o S_o^{v_o} (1 - S_o^{q_o}), \quad (39)$$

where the two sets of the parameters u , v , q have to be determined. The oil saturation term is intended to dominate at small oil saturations, while the water saturation term

should dominate at small water saturations. For mixed-wet conditions, interfacial area may decrease at small water saturations in imbibition because of the displacement from configuration C to D. The interfacial area may start to increase at larger water saturations because of the formation of oil layers in the displacement from configuration C to E. When the oil layers are displaced, interfacial area decreases abruptly. Equation (39) accounts for such behavior since the proposed correlation may yield a local minimum and a local maximum of interfacial area.

[39] To investigate the flexibility of equations (38) and (39), we have fitted the correlations to simulated data. For this purpose we consider the Weibull distributed pore sizes which were employed to simulate the $a_{ow}(S_w)$ curves in Figure 3. We still assume $\sigma_{ow} = 0.050 \text{ N/m}$ and $\theta_{pd} = 0^\circ$ during primary drainage. In the subsequent imbibition and drainage processes, we consider randomly distributed contact angles. For water-wet conditions we assume $\theta_a \in [50^\circ, 80^\circ]$, while for mixed-wet conditions we assume $\theta_a \in [90^\circ, 180^\circ]$. The receding contact angles are calculated by $\theta_r = 0.5\theta_a$ for both water-wet and mixed-wet conditions. The primary drainage curve for the water-wet system is terminated at $P_c^{\max} = 25 \text{ kPa}$, and for the mixed-wet system,

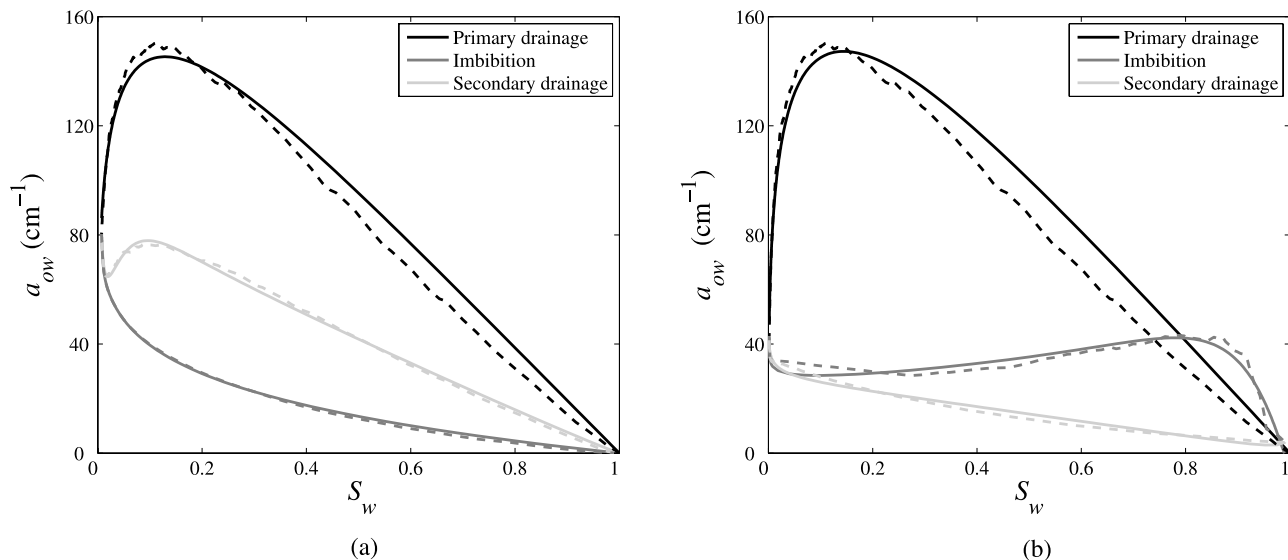


Figure 5. Specific interfacial area plotted against water saturation for primary drainage, imbibition, and secondary drainage. The simulation results are shown by dashed lines, while the proposed correlations fitted to the simulated data are represented by the solid lines. Results are presented for (a) water-wet and (b) mixed-wet conditions.

primary drainage is terminated at $P_c^{\max} = 50$ kPa to facilitate for oil layer formation in the subsequent invasion processes.

[40] Equation (38) is fitted to the primary drainage curve, while equation (39) is fitted to the main imbibition and secondary drainage curves. A standard curve-fitting method is employed to determine the correlation parameters. The results are shown in Figure 5, and the correlations agree fairly well with the simulated data. A better match may be obtained using appropriate error weighting. A comparison between equations (38), (39) and (36) indicates that all parameters are likely to be positive. However, to obtain a good match between the correlations and the simulated data, one or two of the parameters in equation (39) turns out to be slightly negative in some cases.

[41] There is a paucity of measured imbibition and secondary drainage interfacial area data in the literature. However, the imbibition curve in Figure 5b seems to display similar trends as imbibition measurements [Schaefer *et al.*, 2000a, Figure 5]. Nevertheless, more data is required to validate the correlations and to determine the applicability of the model to predict general trends in interfacial area for various conditions.

4. Conjecture of Hassanizadeh and Gray [1993]

[42] To investigate if hysteresis is absent in the $a_{ow} - P_c - S_w$ relationship, as proposed by Hassanizadeh and Gray [1993], we employ our simple bundle of tubes model to perform the same exercise as Held and Celia [2001]. They utilized a network model and generated a drainage a_{ow} surface from drainage scanning curves initiated from different reversal points on the main imbibition curve. Similarly, an imbibition a_{ow} surface was generated by imbibition scanning curves initiated from different reversal points on the main secondary drainage curve. If the intersections of the two surfaces at constant P_c follow the same $a_{ow}(S_w)$ curve, then hysteresis is absent. Held and Celia [2001]

found that the intersections essentially followed the same $a_{ow}(S_w)$ curve, and hence they concluded that the conjecture of Hassanizadeh and Gray [1993] could not be rejected. However, Held and Celia [2001] only considered water-wet media and neglected the contribution of interfacial area from interfaces present in corners of the pore space.

[43] We explore if hysteresis can be eliminated when only interfaces between bulk and corner fluids is contributive to interfacial area. The water-wet and mixed-wet cases modeled in section 3.3 are both examined. After primary drainage, configuration A remains in a few of the smaller tubes. Imbibition is terminated when $S_w = 1$ in the water-wet case. In the mixed-wet case, imbibition is terminated when $S_w = 0.99$. At this stage, configuration E has ceased to exist.

[44] The drainage and imbibition a_{ow} surfaces for the water-wet case are shown in Figures 6a and 6b, respectively, with the bounding hysteresis loop marked by bold lines. The surfaces display a concave-convex shape with scanning curves that may exhibit local minima and local maxima. This clearly deviates from the results of Reeves and Celia [1996] and Held and Celia [2001], who found that the surfaces were convex in both the $a_{ow} - S_w$ and the $a_{ow} - P_c$ plane. The only resemblance is the local convex shape of the drainage surface in the $a_{ow} - S_w$ plane, implying that for any value of capillary pressure there exists at least two points on the surface with different saturations and equal interfacial area. The projections onto the $a_{ow} - S_w$ plane show that the drainage $a_{ow}(S_w)$ scanning curves have a convex shape with a local maximum of a_{ow} at an intermediate value of S_w , and a local minimum at a very small water saturation, which is similar to the secondary drainage curve in Figure 5a. The imbibition surface in Figure 6b are constructed by scanning curves that decreases monotonically with increasing water saturation. This clearly deviates from the results of Reeves and Celia [1996] and Held and Celia [2001]. The sharp decrease of the imbibition a_{ow} surface is caused by the significant contact angle hysteresis

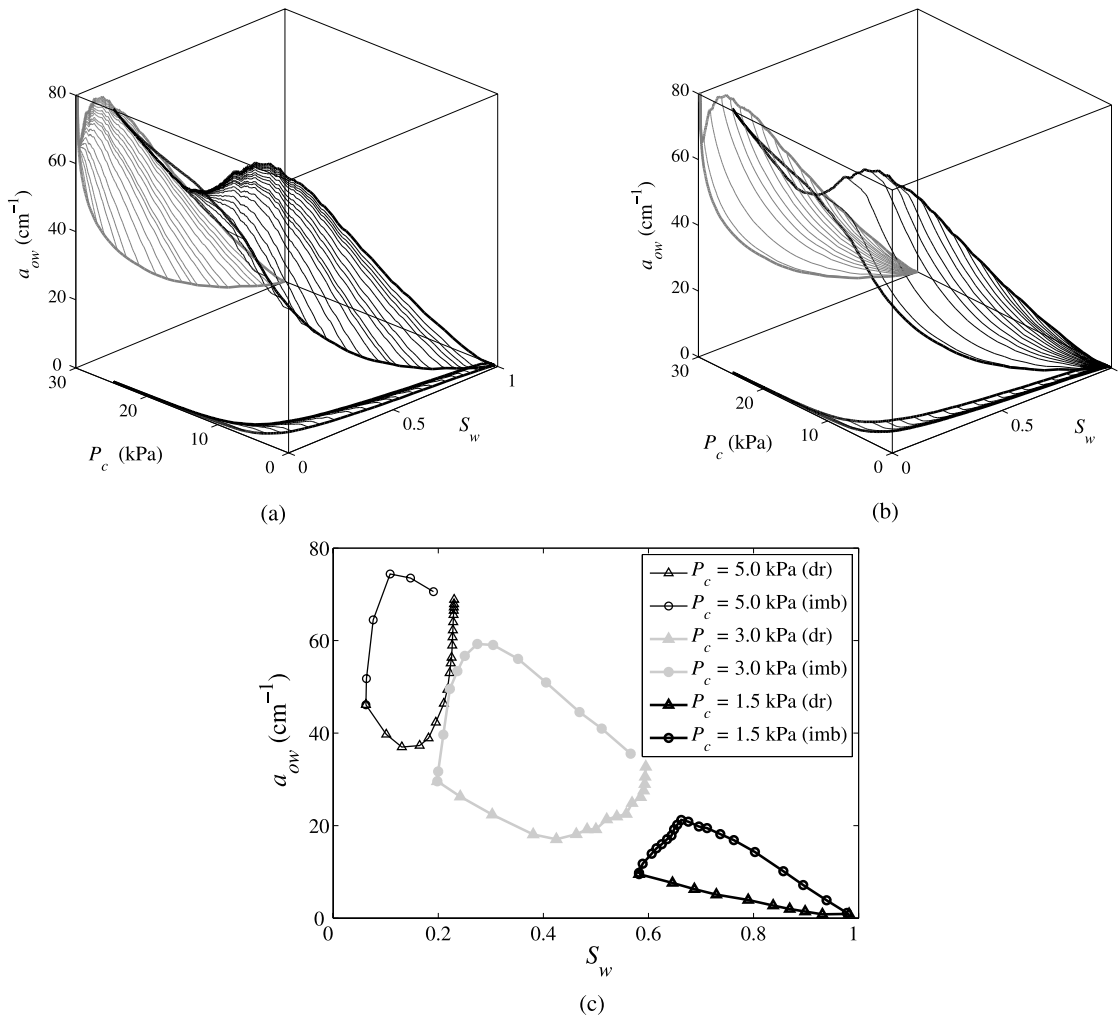


Figure 6. Specific interfacial area a_{ow} plotted as a function of P_c and S_w for water-wet conditions. Projections onto the $P_c - S_w$ plane and $a_{ow} - S_w$ plane are also shown. The bounding hysteresis loop is marked by the bold lines. (a) Surface created by drainage scanning curves. (b) Surface created by imbibition scanning curves. (c) Planes at three constant P_c through the drainage (dr) and imbibition (imb) a_{ow} surfaces.

assumed in our simulations, which causes the interfaces to hinge instead of moving with constant contact angles toward the center of the cross sections prior to piston-like water invasion.

[45] Intersections of the drainage and imbibition a_{ow} surfaces for three constant values of P_c are shown in Figure 6c. Evidently, very different values of specific interfacial area occurs for the different directions of saturation change, implying that hysteresis remains present in the $a_{ow} - P_c - S_w$ relationship. Notice also that the imbibition interfacial area is higher than the drainage interfacial area for a constant value of capillary pressure. We emphasize that this does not imply that interfacial area is higher in imbibition than in drainage for a specific scanning loop. This feature is explained as follows: imbibition scanning curves are initiated from the main secondary drainage curve where interfacial area may be large, while drainage scanning curves are initiated from the main imbibition curve where interfacial area may be small. Because of the significant contact angle hysteresis assumed, the different scanning curves may reach the chosen level of constant capillary pressure before piston-

like invasion results in pronounced changes of interfacial area. The differences between drainage and imbibition interfacial area decreases as water saturation increases. This is due to the shape of the projection of the bounding hysteresis loop in the $a_{ow} - S_w$ plane shown in Figures 6a and 6b.

[46] The corresponding results for the mixed-wet case are presented in Figure 7. The projections onto the $a_{ow} - S_w$ plane reveal that the interfacial area is higher during main imbibition than during main secondary drainage, as opposed to the results for water-wet conditions. The a_{ow} surfaces display a more complex shape for the mixed-wet case because of oil layer formation during imbibition. After primary drainage, the interfaces are hinging until the displacements from configuration C to D occur, resulting in a decrease of interfacial area at small water saturations during imbibition. For larger water saturations, the displacements from configuration C to E occur, resulting in an increased interfacial area. When the interfaces that separate oil layers from bulk water move toward the corners, the interfacial area starts to decrease slightly. Eventually, the oil layers are

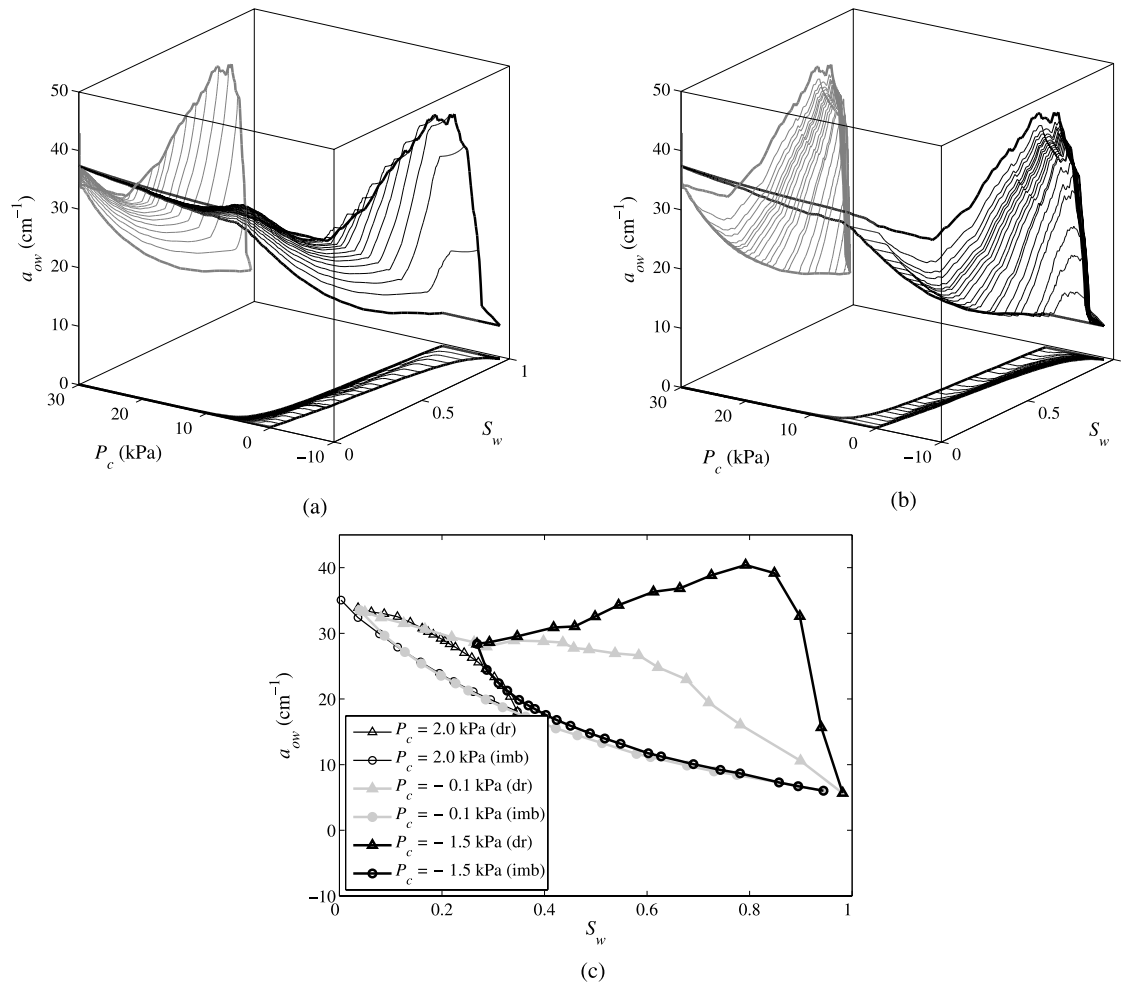


Figure 7. Specific interfacial area a_{ow} plotted as a function of P_c and S_w for mixed-wet conditions. Projections onto the $P_c - S_w$ plane and $a_{ow} - S_w$ plane are also shown. The bounding hysteresis loop is marked by the bold lines. (a) Surface created by drainage scanning curves. (b) Surface created by imbibition scanning curves. (c) Planes at three constant P_c through the drainage (dr) and imbibition (imb) a_{ow} surfaces.

displaced and the interfacial area decreases abruptly. These trends are also present in the imbibition scanning curves, as they display a concave-convex shape with a local minimum and a local maximum. This is demonstrated in Figure 7b. In the drainage processes, the displacement from configuration E to C dominates at intermediate/large water saturations, while the displacement from configuration D to C dominates at small water saturations. Thus the drainage scanning curves display concave shapes in the $a_{ow} - S_w$ plane, as shown in Figure 7a. Following the same reasoning as for the water-wet case, it is expected that the $a_{ow}(S_w)$ curves produced by intersections of the surfaces at constant P_c , result in higher interfacial area in drainage than in imbibition, as shown in Figure 7c. Moreover, the differences between drainage and imbibition interfacial area increases according to the water saturation. This is due to the shape of the projection of the bounding hysteresis loop in the $a_{ow} - S_w$ plane shown in Figures 7a and 7b. Evidently, Figure 7c indicates that hysteresis in the $a_{ow} - P_c - S_w$ relationship remains present for mixed-wet conditions as well.

[47] Gray and Hassanizadeh [1991] and Hassanizadeh and Gray [1993] discuss hysteresis at the pore scale by

means of a tube with circular cross section as the model pore. If contact angle hysteresis is assumed in the pore, the $P_c(S_w)$ curves for drainage and imbibition are different. At a reversal of the displacement process, the main meniscus, which separates the bulk fluids, will hinge while the contact angle changes with capillary pressure according to Young-Laplace's equation, $P_c = 2\sigma_{ow}\cos\theta/R$. The level of the horizontal drainage curve is reached when $\theta = \theta_r$, whereas the lower horizontal imbibition curve is reached when $\theta = \theta_a$. Gray and Hassanizadeh [1991] and Hassanizadeh and Gray [1993] argue that the apparent hysteresis in the capillary pressure curves arise because of the choice of only S_w as the independent variable. While the $a_{ow} - S_w$ and $P_c - S_w$ relationships for the cylindrical tube clearly exhibit hysteresis, the relationship $a_{ow} - P_c$ is unique. A consequence of this is that no hysteresis will be present in the full $a_{ow} - P_c - S_w$ relationship. The interfacial area of the meniscus in the cylindrical pore is given by

$$A_{ow}^{cyl} = \pi \left\{ 2R^2 + \left[\frac{2\sigma_{ow}}{P_c} \right]^2 \left(1 - \sin \left(\arccos \left[\frac{P_c R}{2\sigma_{ow}} \right] \right) \right)^2 \right\}, \quad (40)$$

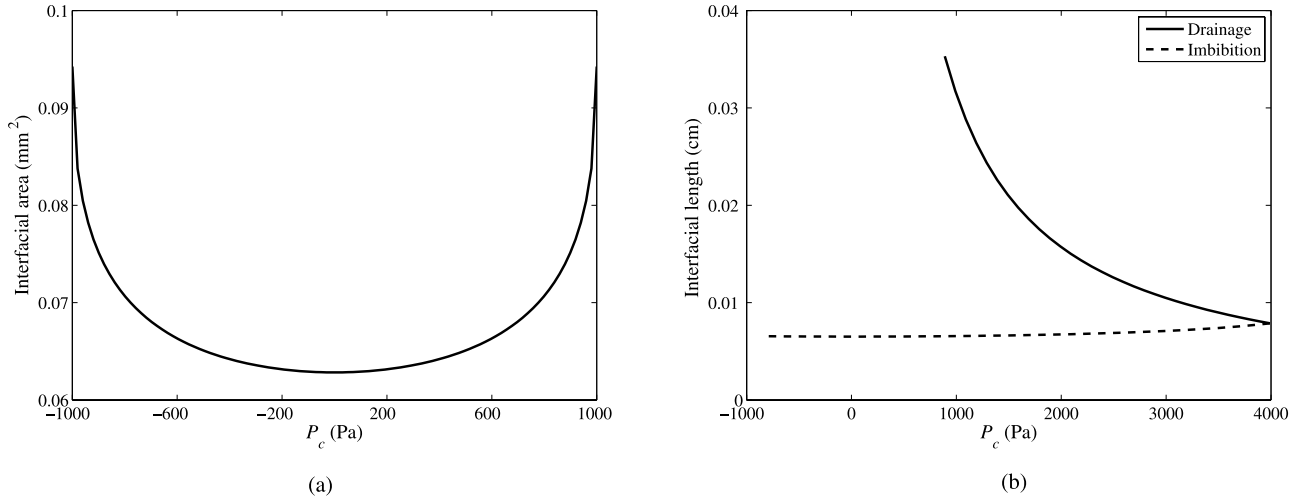


Figure 8. (a) Interfacial area plotted as a function of capillary pressure for a main meniscus in a cylindrical pore of circular cross section. (b) Total length of the interfaces in the corners of a triangular pore cross section plotted as a function of capillary pressure for drainage and imbibition.

where the contact angles are eliminated using Young-Laplace's equation. In Figure 8a, we have plotted interfacial area versus capillary pressure for a cylindrical tube with radius $R = 100 \mu\text{m}$ and contact angles $\theta_r = 0^\circ$ and $\theta_a = 180^\circ$. The result is a U-shaped curve with a minimum at zero capillary pressure corresponding to a flat interface. The endpoint values represent the capillary pressures at the receding and advancing contact angles, which correspond to meniscus movement, i.e., the horizontal parts of the drainage and imbibition $P_c(S_w)$ curves.

[48] We have demonstrated that the $a_{ow} - S_w$ and $P_c - S_w$ relationships calculated from a model of triangular pore cross sections exhibit hysteresis. More interestingly, hysteresis remains present in the $a_{ow} - P_c$ relationship from the triangular pore model when contact angle hysteresis is assumed, as opposed to the cylindrical pore. To demonstrate this, consider a drainage scenario where the interfaces that formed after piston-like oil invasion move toward the corners as the capillary pressure increases. This displacement occurs with a constant receding contact angle according to equation (13). Obviously, the lengths of the interfaces must decrease during this process because of the converging corner geometry. When the displacement process is reversed, the contact line becomes pinned and the contact angle changes with capillary pressure according to equation (12), which leads to a further reduction of the interfacial length. In Figure 8b, the interfacial lengths are plotted as a function of capillary pressure for drainage and imbibition in a pore with inscribed radius $R = 100 \mu\text{m}$ and contact angles $\theta_r = 0^\circ$ and $\theta_a = 180^\circ$. The difference in capillary behavior for the drainage and imbibition processes leads to a hysteretic and nonunique $a_{ow}(P_c)$ function. Consequently, hysteresis remains present in the full $a_{ow} - P_c - S_w$ relationship as well. Our model does not account for the main meniscus between the bulk fluids. On the basis of the analysis of the cylindrical tube, one might expect that the contribution of the interfacial area from the main meniscus may eliminate the hysteresis in the $a_{ow} - P_c - S_w$ relationship in a three-dimensional representation of the tube with triangular cross section. However, in a three-dimensional model, the cross

section along the tube length may vary, and one can easily imagine that the capillary behavior of hinging and moving interfaces, which were demonstrated in Figure 8b for the pore corners, can occur for the main meniscus as well because of converging or diverging pore geometry. Thus, when contact angle hysteresis occurs, the conjecture by *Hassanzadeh and Gray* [1993] seems to be valid only in very simple idealized pore shapes, such as the cylindrical tube of circular cross section. From the above considerations, it seems that hysteresis at the pore scale generally results in hysteresis at the larger scale, even though interfacial area is included as an independent variable in the capillary pressure versus saturation relationship.

5. Summary and Conclusions

[49] We have used a simple bundle of triangular tubes model to calculate specific interfacial area as a function of saturation for primary drainage, imbibition and secondary drainage for mixed-wet conditions. The model employs accurate expressions for the capillary entry pressures, accounting for the possibility of hinging interfaces in the corners due to contact angle hysteresis. Analytical expressions for specific interfacial area as a function of saturation and capillary pressure are derived for primary drainage, assuming that only the interfaces between bulk and corner fluid is contributive to interfacial area. Flexible correlations are suggested for the subsequent imbibition and secondary drainage processes. We have also investigated if hysteresis occurs in the relationship between capillary pressure, saturation and interfacial area.

[50] The specific conclusions are as follows:

[51] 1. The simulation results show that very different trends in the specific interfacial area versus saturation curves can occur during imbibition, depending on the reversal point after primary drainage and the advancing contact angle. For water-wet conditions, interfacial area scanning curves coincide with the bounding imbibition curve, while for oil-wet conditions the scanning curves may cross each other because of the impact hinging inter-

faces in the corners have on the invasion order of the pore sizes.

[52] 2. The analytically derived correlations imply that the capillary pressure versus saturation relationship and the interfacial area versus saturation relationship are equivalent in primary drainage of triangular tubes.

[53] 3. The proposed correlations are in agreement with the interfacial area data generated by the model. Experimental measurements of hysteresis loops are required to validate the correlations and to determine the applicability of the model for interfacial area calculations.

[54] 4. Hysteresis in the relationship between capillary pressure, saturation and corner fluid–bulk fluid interfacial area remains present between imbibition and secondary drainage processes if contact angle hysteresis is assumed. Hysteresis may be significant for both water-wet and mixed-wet conditions. A more sophisticated model is required to investigate if this is also the case when the hysteresis is caused by phase entrapment and snap-off events.

Notation

A	cross-sectional area.
a	specific interfacial area.
b	position of arc meniscus.
dA_{ij}	change in interfacial area between phases i and j .
dF	change in surface free energy.
dF_H	change in Helmholtz free energy.
dV_i	change in volume of phase i .
f	pore size density.
g_1	geometry factor; see equation (27).
g_2	geometry factor; see equation (28).
I	indicator notation; see equation (6).
L_s	cross-sectional fluid–solid length.
L_f	cross-sectional fluid–fluid length.
N	total number of interfaces present in a corner.
P	pressure.
q	correlation parameter; see equations (38) and (39).
r	radius of curvature.
R	radius of the inscribed circle.
S	saturation.
\mathcal{S}	total area of interfaces within a representative volume.
u	correlation parameter; see equations (38) and (39).
\mathcal{V}	representative volume.
v	correlation parameter; see equations (38) and (39).
W	virtual work.
x	random number between 0 and 1.
α	corner half angle.
β	angle defined from geometry of the interfaces in the corners; see equation (11).
ϵ	geometry factor; see equation (26).
η	parameter in the Weibull distribution.
θ	contact angle.
ν	parameter in pore size distribution.
σ	interfacial tension.
ψ	angle.

Subscripts

a	advancing.
b	bulk.
c	corner or capillary.
ch	characteristic.
h	hinging.
o	oil.
pd	primary drainage.
r	receding.
s	solid.
w	water.

Superscripts

cyl	cylinder.
fin	final.
$init$	initial.
(k)	interface number counted in order from corner toward center.

[55] **Acknowledgments.** The authors thank Rink van Dijke and Ken Sorbie for many discussions on the topic of two- and three-phase entry pressures. Support for Johan Olav Helland was provided by Statoil through the VISTA program.

References

- Bradford, S. A., and F. J. Leij (1997), Estimating interfacial areas for multi-fluid soil systems, *J. Contam. Hydrol.*, 27, 83–105.
- Brooks, R. H., and A. T. Corey (1964), Hydraulic properties of porous media, *Hydraul. Pap.* 3, Colo. State Univ., Fort Collins, Colo.
- Dalla, E., M. Hilpert, and C. T. Miller (2002), Computation of the interfacial area for two-fluid porous medium systems, *J. Contam. Hydrol.*, 56, 25–48.
- Dillard, L. A., H. I. Essaid, and M. J. Blunt (2001), A functional relation for field-scale nonaqueous phase liquid dissolution developed using a pore network model, *J. Contam. Hydrol.*, 48, 89–119.
- Dong, M., F. A. L. Dullien, and I. Chatzis (1995), Imbibition of oil in film form over water present in edges of capillaries with an angular cross section, *J. Colloid Interface Sci.*, 172, 21–36.
- Faisal Anwar, A. H. M., M. Bettahar, and U. Matsubayashi (2000), A method for determining air–water interfacial area in variably saturated porous media, *J. Contam. Hydrol.*, 43, 129–146.
- Gladkikh, M., and S. Bryant (2003), Prediction of interfacial areas during imbibition in simple porous media, *Adv. Water Resour.*, 26, 609–622.
- Gray, W. G. (1999), Thermodynamics and constitutive theory for multi-phase porous-media flow considering internal geometric constraints, *Adv. Water Resour.*, 22, 521–547.
- Gray, W. G., and S. M. Hassanizadeh (1991), Paradoxes and realities in unsaturated flow theory, *Water Resour. Res.*, 27(8), 1847–1854.
- Hassanizadeh, S. M., and W. G. Gray (1993), Thermodynamic basis of capillary pressure in porous media, *Water Resour. Res.*, 29(10), 3389–3405.
- Held, R., and M. A. Celia (2001), Modeling support of functional relationships between capillary pressure, saturation, interfacial area and common lines, *Adv. Water Resour.*, 24, 325–343.
- Helland, J. O., and S. M. Skjæveland (2006), Physically-based capillary pressure correlation for mixed-wet reservoirs from a bundle-of-tubes model, *SPE J.*, 11(2), 171–180.
- Hui, M., and M. J. Blunt (2000), Effects of wettability on three-phase flow in porous media, *J. Phys. Chem. B*, 104, 3833–3845.
- Kennedy, C. A., and W. C. Lennox (1997), A pore-scale investigation of mass transport from dissolved DNAPL droplets, *J. Contam. Hydrol.*, 24, 221–246.
- Kovscek, A. R., H. Wong, and C. J. Radke (1993), A pore-level scenario for the development of mixed wettability in oil reservoirs, *Am. Inst. Chem. Eng. J.*, 39(6), 1072–1085.
- Ma, S., G. Mason, and N. R. Morrow (1996), Effect of contact angle on drainage and imbibition in regular polygonal tubes, *Colloids Surf. A*, 117, 273–291.
- Morrow, N. R. (1970), Physics and thermodynamics of capillary action in porous media, *Ind. Eng. Chem.*, 62(6), 32–56.
- Morrow, N. R. (1975), The effects of surface roughness on contact angle with special reference to petroleum recovery, *J. Can. Pet. Technol.*, 14(4), 42–53.

- Oostrom, M., M. D. White, and M. L. Brusseau (2001), Theoretical estimation of free and entrapped nonwetting-wetting fluid interfacial areas in porous media, *Adv. Water Resour.*, 24, 887–898.
- Or, D., and M. Tuller (1999), Liquid retention and interfacial area in variably saturated porous media: Upscaling from single-pore to sample-scale model, *Water Resour. Res.*, 35(12), 3591–3605.
- Øren, P., S. Bakke, and O. Arntzen (1998), Extending predictive capabilities to network models, *SPE J.*, 3(4), 324–336.
- Paterson, A., M. Robin, M. Fermigier, P. Jenffer, and J. P. Hulin (1998), Effect of density and spatial distribution of wettability heterogeneities on contact angle, *J. Pet. Sci. Eng.*, 20, 127–132.
- Piri, M., and M. J. Blunt (2005), Three-dimensional mixed-wet random pore-scale network modeling of two- and three-phase flow in porous media: I. Model description, *Phys. Rev. E*, 71, 026301.
- Reeves, P. C., and M. A. Celia (1996), A functional relationship between capillary pressure, saturation and interfacial area as revealed by a pore-scale network model, *Water Resour. Res.*, 32(8), 2345–2358.
- Saripalli, K. P., P. S. C. Rao, and M. D. Annable (1998), Determination of specific NAPL-water interfacial areas of residual NAPLs in porous media using the interfacial tracers technique, *J. Contam. Hydrol.*, 30, 375–391.
- Schaefer, C. E., D. A. DiCarlo, and M. J. Blunt (2000a), Experimental measurement of air-water interfacial area during gravity drainage and secondary imbibition in porous media, *Water Resour. Res.*, 36(4), 885–890.
- Schaefer, C. E., D. A. DiCarlo, and M. J. Blunt (2000b), Determination of water-oil interfacial area during 3-phase gravity drainage in porous media, *J. Colloid Interface Sci.*, 221, 308–312.
- Schäfer, A., P. Ustohal, H. Harms, F. Stauffer, T. Dracos, and A. J. B. Zehnder (1998), Transport of bacteria in unsaturated porous media, *J. Contam. Hydrol.*, 33, 149–169.
- van Dijke, M. I. J., and K. S. Sorbie (2006), Existence of fluid layers in the corners of a capillary with non-uniform wettability, *J. Colloid Interface Sci.*, 293, 455–463.
- van Genuchten, M. T. (1980), A closed-form equation for predicting the hydraulic conductivity of unsaturated soils, *Soil Sci. Soc. Am. J.*, 44, 892–898.

J. O. Helland, International Research Institute of Stavanger, P.O. Box 8046, N-4068 Stavanger, Norway. (johan.olav.helland@iris.no)

S. M. Skjæveland, Department of Petroleum Engineering, University of Stavanger, N-4013 Stavanger, Norway. (s-skj@ux.uis.no)